JACS
JOURNAL OF THE AMERICAN CHEMICAL SOCIETY

Article

pubs.acs.org/JACS

Unexpected High-Temperature Stability of β-Zn_4Sb_3 Opens the Door to Enhanced Thermoelectric Performance

Jianping Lin,[†] Xudong Li,[‡] Guanjun Qiao,*[,†,§] Zhao Wang,*[,‡] Jesús Carrete,[∥] Yang Ren,[⊥] Lingzhi Ma,[†] Youjian Fei,[†] Baifeng Yang,[†] Lei Lei,[†] and Ju Li*[,‡,#]

[†]State Key Laboratory for Mechanical Behavior of Materials and [‡]Frontier Institute of Science and Technology, Xi'an Jiaotong University, Xi'an, 710049, P. R. China

[§]School of Materials Science and Engineering, Jiangsu University, Zhenjiang, 212013, P. R. China

[∥]CEA-Grenoble, Grenoble 38000, France

[⊥]X-ray Science Division, Advanced Photon Source, Argonne National Laboratory, Argonne, Illinois 60439, United States

[#]Department of Nuclear Science and Engineering and Department of Materials Science and Engineering, Massachusetts Institute of Technology, Cambridge, Massachusetts 02139, United States

ABSTRACT: β-Zn_4Sb_3 has one of the highest ZT reported for binary compounds, but its practical applications have been hindered by a reported poor stability. Here we report the fabrication of nearly dense single-phase β-Zn_4Sb_3 and a study of its thermoelectric transport coefficients across a wide temperature range. Around 425 K we find an abrupt decrease of its thermal conductivity. Past this point, Zn atoms can migrate from crystalline sites to interstitial positions; β-Zn_4Sb_3 becomes metastable and gradually decomposes into Zn(hcp) and ZnSb. However, above 565 K it recovers its stability; in fact, the damage caused by decomposition can be repaired completely. This is key to its excellent thermoelectric performance at high temperature: the maximum ZT reaches 1.4. Molecular dynamics simulations are used to shed light on the microscopic behavior of the material.

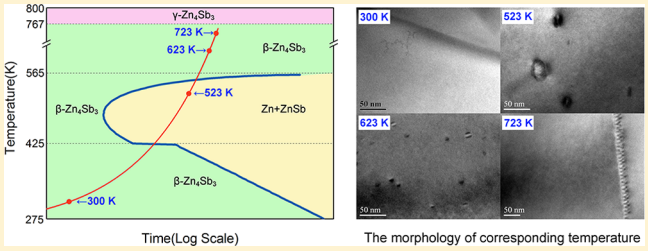

INTRODUCTION

So far, thermoelectric (TE) energy conversion has been mostly confined to niche applications, such as spot cooling and space exploration, due to its limited efficiency. TE efficiency is known to be bounded by a monotonically increasing function of $ZT = S^2T/\rho(\kappa_e + \kappa_L)$, where S is the Seebeck coefficient, ρ the electrical resistivity, κ_e and κ_L the electronic and lattice contributions to thermal conductivity, and T the absolute temperature. In theory, there is no upper limit to ZT,[1] but high ZT values above 1.3 are rare and usually found in superlattices[2,3] and low-dimensional[4] or nanostructured materials.[5−8] In those cases, ease of fabrication, costs, and environmental friendliness can be causes of concern. On the other hand, among all binary TE materials discovered to date, β-Zn_4Sb_3 is one of those with the lowest thermal conductivity and highest ZT at intermediate temperatures. It also has the advantage of not depending on tellurium; antimony, though not as plentiful as zinc, is 200 times more abundant in the Earth's crust.[9]

Stability is a key requirement for a candidate thermoelectric material, so it is not surprising that a lot of effort has been devoted to its study.[10−12] It is known that β-Zn_4Sb_3 transforms into α- or α'-Zn_4Sb_3 below 263 K and into γ-Zn_4Sb_3 above 765 K; in both cases the transformations are accompanied by a significant degradation in ZT. Hence, the optimal temperature range for this material should be between 263 and 765 K. However, even within this interval the stability of β-Zn_4Sb_3 is often called into question; in fact, *ab initio* calculations indicate that there might be a small thermodynamic driving force for

$$\beta\text{-}Zn_4Sb_3 \rightarrow Zn(hcp) + ZnSb \quad (1)$$

decomposition below $T_{thermo} \sim 700$ K,[13,14] although this T_{thermo} value may not be quantitative due to limited calculation accuracy. Some studies have proposed a starting temperature of 500 K[15−17] for decomposition into ZnSb and Zn,[15,18,19] but instabilities below 500 K have also been reported.[15,20] On the other hand, there are experimental reports of an outstanding ZT of about 1.3 at around 670 K.[21,22] Measurements of ZT in the temperature range between 670 and 765 K have not been reported to date, although the almost linear increase in performance with T in β-Zn_4Sb_3 suggests it should be optimal. Thus, there is an important gap in the available experiments due to the unavailability of good samples.

In this paper we measure a continuous ZT vs T curve extending beyond the maximum temperature of previous reports and reaching a ZT around 1.4. We find an abrupt decrease of thermal conductivity around 425 K, where the Rietveld refinement shows that Zn atoms migrate from normal to interstitial sites, making β-Zn_4Sb_3 metastable. We address the thermodynamic stability and transformation kinetics of β-

Received: October 16, 2013
Published: December 23, 2013

   dx.doi.org/10.1021/ja410605f | J. Am. Chem. Soc. 2014, 136, 1497−1504

Zn_4Sb_3 and find that it becomes stable after 565 K; this is the basis of its high thermoelectric performance. We confirm these findings by means of molecular dynamics (MD) simulations.

EXPERIMENTAL SECTION

Flux-grown crystals of the material commonly referred to as "β-Zn_4Sb_3" have in fact a composition close to $Zn_{13}Sb_{10}$.[18] Due to the evaporation of Zn during sintering, compositions need to be slightly Zn rich. Here, a group of samples were synthesized at different starting average compositions. The nominally single-phase (SP) sample has a starting Zn composition of 56.90 at. %, which corresponds to $Zn_{1.320}Sb$. For comparison, we also synthesized a zinc-rich (ZR) sample, with a starting Zn composition of 57.14 at. % ($Zn_{1.333}Sb$), which we later show to be clearly multiphase. The densities of both samples are close to the conventional value (SP: 6.34 g/cm^3, ZR: 6.35 g/cm^3, conventional density:[23] 6.36 g/cm^3). The compounds were prepared from 99.999% purity zinc shots and 99.99% purity antimony powder. These elements were loaded into a quartz ampule and sealed under vacuum down to 10^{-4} Torr. After sealing, the ampules were heated to 1023 K at a rate of 375 K/h and kept at that temperature for 72 h; in order to achieve uniform mixing, we rotated the mixtures continuously during the whole process. Finally, they were quenched in cold water. The resulting ingots were ground in an agate mortar and sieved. Powders of 48 μm or less were loaded into graphite dies and sintered by a plasma-activated sintering (PAS) system at 100 MPa and 723 K for 5 min. The sintered samples were cut into several pieces for physical measurements using a spark erosion cutter. To test that reaction (1) reverses direction above 565 K, 75 at. % ZnSb powders and 25 at. % Zn powders were mixed and pressed into tablet form. Then, the tablets were heated to the specific temperature and held for 1 h under argon. The resulting tablets were ground to powder and analyzed by X-ray diffraction (XRD). The SP samples as well as the mixtures were analyzed by differential scanning calorimetry (DSC). Some SP samples were heated at different temperatures (523, 623, 723 K) for 5 h under an argon atmosphere and then quickly cooled down. After such heat treatment the samples were analyzed by high-resolution transmission electron microscopy (HRTEM). Electrical resistivities (ρ) and Seebeck coefficients (S) were measured using a Linseis Seebeck coefficient/electric resistance measuring system (LSR-3), whereas thermal diffusivities (α) and specific heats (C_p) were obtained using a laser flash apparatus (NETZSCH LFA 457). The latter two variables were used to calculate the thermal conductivity (κ) from the relationship:

$$\kappa = \rho_m \alpha C_p \tag{2}$$

where ρ_m is the mass density. The electronic contribution to the total thermal conductivity (κ_e) was estimated from the Wiedemann–Franz law as $\kappa_e = LT/\rho$, and the lattice thermal conductivity (κ_L) extracted as $\kappa_L = \kappa - \kappa_e$. The Lorenz number ($L$) was estimated from the reduced chemical potential η. This method is more accurate than simply using the nominal value of this constant and is recommended by previous studies.[24−27] In turn, η was obtained from the Seebeck coefficient S. More specifically, the relevant equations are

$$S = \frac{k_B}{e}\left[\frac{2F_1(\eta)}{F_0(\eta)} - \eta\right] \tag{3}$$

and

$$L = \left(\frac{k_B}{e}\right)^2 \frac{3F_0(\eta)F_2(\eta) - 4F_1(\eta)^2}{F_0(\eta)^2} \tag{4}$$

where k_B is the Boltzmann constant, e is the elementary charge, and $F_n(\eta)$ is the order-n Fermi integral defined by May et al:[24]

$$F_n(\eta) = \int_0^{+\infty} x^n (e^{x-\eta} + 1)^{-1} dx \tag{5}$$

This calculation assumes a single-parabolic-band model and a dominant role of acoustic phonons in electronic scattering.

X-ray experiments to study the structure of the samples at high temperatures were carried out at the beamline 11-ID-C of the Advanced Photon Source at Argonne National Laboratory. Room-temperature results are shown in Figure 1. High-energy X-rays

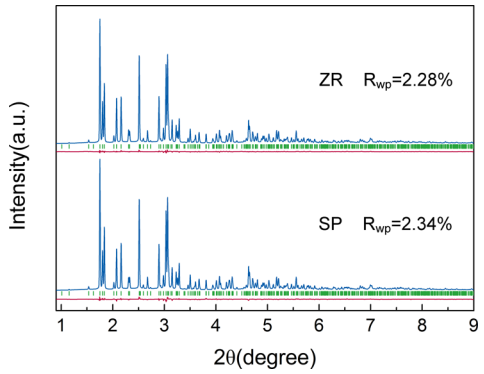

Figure 1. High-energy X-ray powder diffraction data of β-Zn_4Sb_3 at room temperature. Vertical green bars: Bragg peaks of β-Zn_4Sb_3. Red lines: difference between observed and calculated data.

(wavelength λ = 0.10798 Å) penetrate through the cut samples (pellets 1 mm thick and 5 mm in diameter), probing the bulk structures. A Linkam high-temperature stage was used for the temperature-dependent measurements with samples protected in argon during heating. Data were collected in the transmission geometry using a 2D area detector from 300 to 750 K, with a step size of 25 K and a ramp rate of 10 K/min. The stabilization time was 0.5 min, and the data collection time was 1 min (total 3 min/data point). 2D patterns were converted to conventional diffraction data (intensity vs 2Θ) using the FIT2D software package.[28] The GSAS program was used for the Rietveld refinement.[29] The space group is $R\bar{3}c$ (167) with a = 12.24175(7) and c = 12.44274(9) Å (SP sample) at room temperature. The minimum weighted profile factor (R_{wp}) is 2.28% for ZR at 300 K, and the maximum R_{wp} is 2.84% for SP at 750 K.

RESULTS AND DISCUSSION

Samples with slightly different initial compositions show significant differences in electrical resistivity and Seebeck coefficient (Figure 2a,b). ρ(SP) and ρ(ZR) both increase with increasing temperature from 300 to 400 K, but the ZR sample has a saddle point at about 425 K which is absent from the ρ(SP) curve; on the other hand, when T reaches 550 K, ρ(SP) reaches a local maximum and begins to drop slowly, possibly due to the onset of ambipolar conduction, but ρ(ZR) keeps on rising continuously until 693 K—the melting point of Zn(hcp)—and then suddenly drops because the free Zn(hcp) phase in ZR sample starts to melt. Presumably, the Zn liquid metal starts to link up into percolating paths along the grain boundaries to reduce ρ(ZR). Although high-energy X-ray powder diffraction shows no obvious difference in composition between SP and ZR (Figure 1), the transport properties confirm the clear difference in composition. These results indicate that small amounts Zn(hcp) in β-Zn_4Sb_3 change its transport properties. It must be noted that the stability of the SP sample was verified by measuring its resistivity two times, upon which two almost overlapping curves were obtained. The value of ρ and its trends reported in ref 30 are more similar to those of ρ(ZR), which possibly means that the sample in ref 30 contained excess Zn(hcp). Similar patterns are observed in the Seebeck coefficient plot. S(ZR) and the S in ref 30 both have a turning point at around 450 K. Similarly, the two S(SP) curves almost overlap. The difference between S(SP) and S(ZR) is

dx.doi.org/10.1021/ja410605f | J. Am. Chem. Soc. 2014, 136, 1497−1504

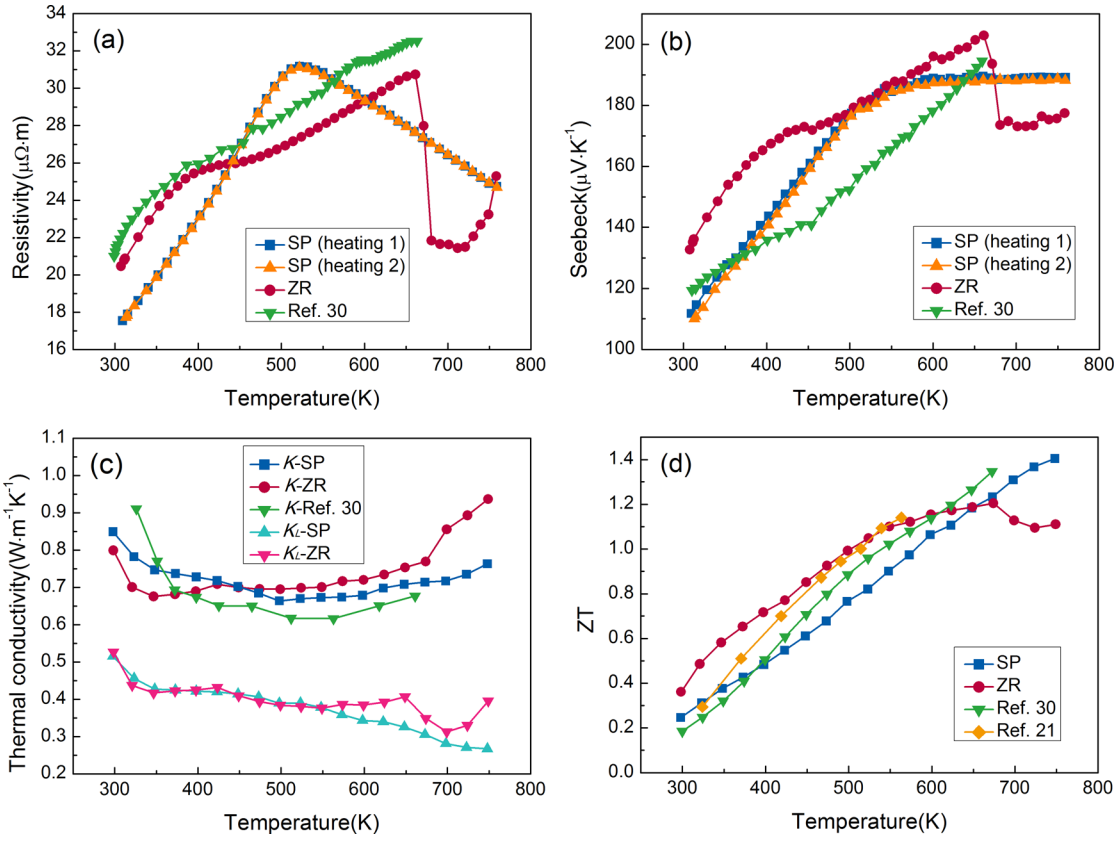

Figure 2. Transport properties of bulk β-Zn_4Sb_3 samples as a function of temperature: (a) resistivity, (b) Seebeck coefficient, (c) Thermal conductivity (κ) and lattice thermal conductivity (κ_L), and (d) ZT and comparison with data from the literature.

that S(SP) remains flat after 550 K, in contrast to the drop in ρ(SP); this is clearly beneficial for the figure of merit. The maximum Seebeck coefficient of SP (189 μV/K) is a bit smaller than that of ZR (202 μV/K) and in line with previous reports.[21,22]

Low thermal conductivity is crucial to high-performance bulk TE materials. β-Zn_4Sb_3 is one of the most efficient TE materials at moderate temperature due to its exceptionally low thermal conductivity. As shown in Figure 2c, the temperature dependence of κ(SP) and κ(ZR) is quite different, with the main minima of both curves located away from each other, and leading to the wider thermal conductivity gap between SP and ZR after 500 K. Remarkably, the thermal conductivity of the SP sample at the minimum is 0.66 W/(m·K), close to the armorphous limit. But κ(SP) is still higher than the κ reported in ref 30 in the interval 400−673 K. After 693 K, κ(ZR) increases rapidly due to the melting of excess Zn. A more detailed analysis reveals that the decline of κ can be traced mainly to κ_L. After 425 K, κ_L(SP) continues to decline up to the point where the phase transition occurs, but κ_L(ZR) increases slightly after 550 K. Hence, small compositional changes lead to big differences in κ_L. This raises some important questions: What is the cause of the decline of κ_L after 425 K? What is the reason leading to the slight increase of κ_L(ZR)? These are discussed later in the article.

As a consequence of these contrasts, there is a crossover between ZT(ZR) and ZT(SP) at 625 K, as reflected in Figure 2d. Above this temperature, the aforementioned melting of excess Zn prevents any further increase of ZT(ZR). This clear difference between ZT(ZR) and ZT(SP) illustrates the fact that minute changes in composition (0.24 at. % more Zn in this case) can be critical to TE performance; therefore, obtaining stable, high-quality materials with optimized compositions is of the utmost importance for practical applications. The maximum ZT of our ZR sample is 1.2 at 674 K, close to that of ref 21 (thin film) at 550 K. However, the ZT of our SP sample can reach 1.4 at 748 K. When examined in the context of other values reported in the literature, such ZT(SP) is lower than ref 30 above 400 K; however, our measurements show that it is still very good past 693 K, a conclusion not supported by any previously published measurement to the best of our knowledge. It can be speculated that the melting of Zn and its possible evaporation from low-density samples are two possible reasons for this.

As mentioned above, the thermal conductivity of our SP sample is exceptionally low for a crystalline system, always below 0.75 W/(m·K) in the temperature range from 400 to 700 K. In order to shed light on this issue, we refined the XRD data collected at different temperatures. The emerging picture of the structure of room-temperature β-Zn_4Sb_3 is shown in Figure 3a, and Zn(1)−Sb(1) as well as Sb(2)−Sb(2) bonds are depicted in Figure 3b. We characterize the structural evolution of this atomic arrangement by its lattice volume, site occupancies, and bond lengths as functions of temperature. The first derivative of the lattice volume of β-Zn_4Sb_3, also shown in Figure 3c, implies that the thermal expansion coefficient increases with temperature up to 425 K. Likewise, the occupancy of Zn(1) (Figure 3d) rises from room temperature to 425 K. This can be understood in connection with β-Zn_4Sb_3 being a non-equilibrium configuration at room temperature: the cooling rate after PAS sintering is very high, and equilibrium cannot be reached through migration of Zn atoms in the short time that it

dx.doi.org/10.1021/ja410605f | J. Am. Chem. Soc. 2014, 136, 1497−1504

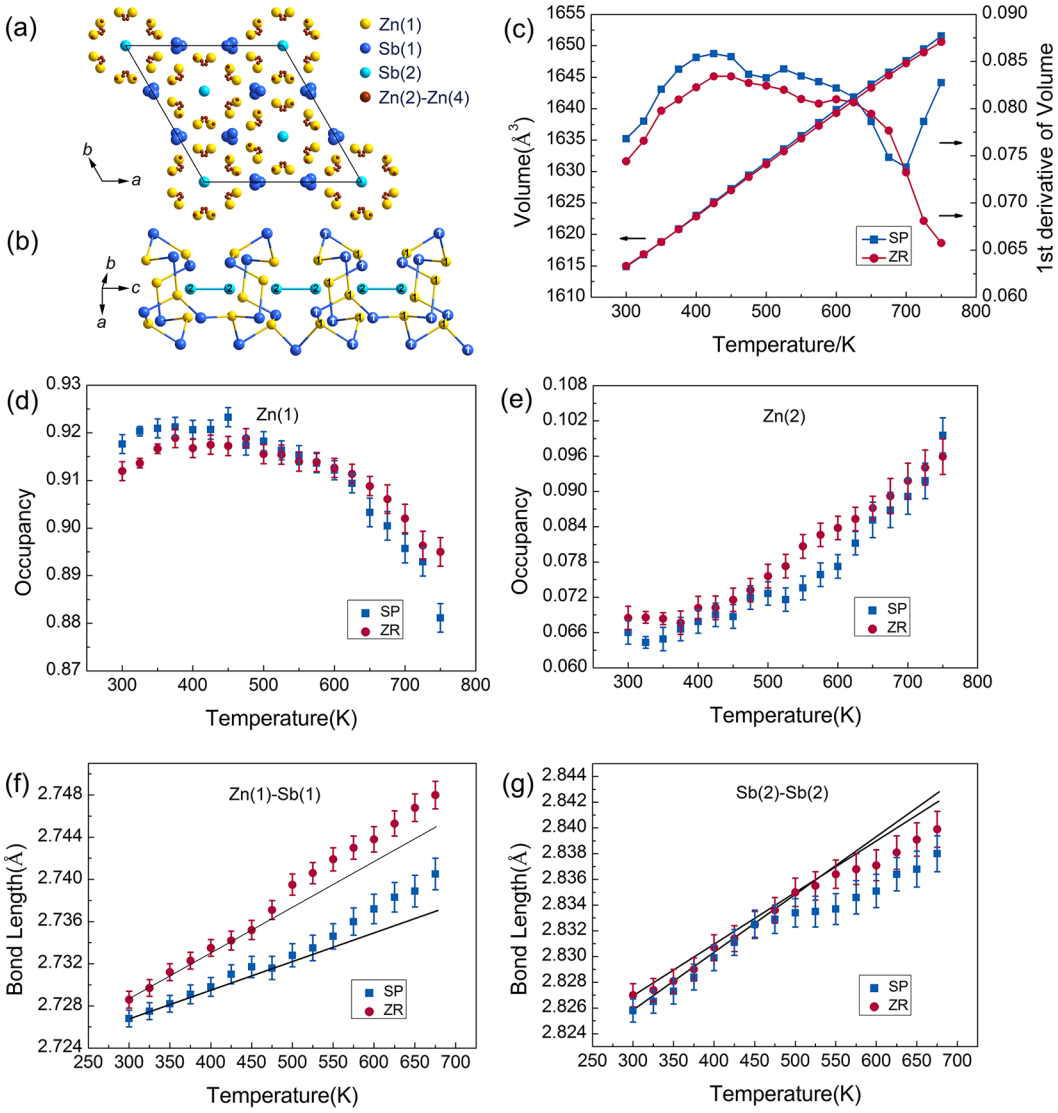

Figure 3. Structural characterization of β-Zn_4Sb_3: (a) refined structure of room-temperature β-Zn_4Sb_3; (b) illustration of Zn(1)−Sb(1) and Sb(2)−Sb(2) bonds; (c) lattice volume of β-Zn_4Sb_3 as a function of temperature and first derivative thereof; (d) occupancy of Zn(1) site; (e) occupancy of Zn(2) sites; (f) Zn(1)−Sb(1) bond length; and (g) Sb(2)−Sb(2) bond length.

takes the sample to reach room temperature. In contrast, from 425 to 693 K (melting point of Zn), the thermal expansion coefficient is gradually reduced, and the occupancy of Zn(1) continuously decreases in favor of the occupancy of interstitial Zn(2) sites (Figure 3e). That means that more and more Zn atoms migrate from Zn(1) sites to interstitial Zn(2) sites when T is increased. Although crucial for understanding the behavior of this material, the effect is subtle in quantitative terms: the decrease in Zn(1) occupancy is 0.4% in the SP sample and just 0.18% in the ZR sample when going from 425 to 525 K (Figure 3d). This different relative importance has a direct effect on the lattice thermal conductivity, which experiences a greater drop for the SP sample (Figure 2c). Furthermore, we can conclude that the increase of Zn(1) vacancies and interstitial atoms leads to the drop in κ_L after 425 K.

To further analyze atomic migration, we focus on the bond length of Zn(1)−Sb(1) as shown in Figure 3f. The bond length of Zn(1)−Sb(1) grows faster above ∼425 K, a sign of an increased instability of Zn(1)−Sb(1) bonds. Hence, the decrease in occupancy of Zn(1) is caused by more bonds breaking past this 425 K point. It is interesting to note that the Sb(2)−Sb(2) and Zn(1)−Sb(1) bond length curves show opposite trends; indeed, the slope of the Sb(2)−Sb(2) is lower after about 425 K (Figure 3g), a hint that Sb(2)−Sb(2) dimers become more stable.

To understand in further detail how this remarkably low thermal conductivity is achieved, we also performed MD simulations of β-Zn_4Sb_3 at different temperatures. The parallel MD simulator LAMMPS was used.[31] The complex hexagonal structure of β-Zn_4Sb_3[32] was reproduced in 3D with the experimentally measured Zn/Sb atom ratio in the Zn-rich samples[23,33,34] (Figure 4a). Our simulation box contained 12 × 12 × 12 unit cells with periodic boundary conditions applied in all three orthogonal directions. The equations of motion were integrated using the Verlet algorithm with a time step of 0.5 fs. A Nosé−Hoover thermostat was used to help the system reach thermal equilibrium at different temperatures before performing any statistical analysis. The atomic interactions were described by a three-body potential successfully applied in the past to the study of β-Zn_4Sb_3 mechanical behaviors.[35] We tested the accuracy of our MD approach by simulating the typical β−α phase transition of this material and computing its

dx.doi.org/10.1021/ja410605f | J. Am. Chem. Soc. 2014, 136, 1497−1504

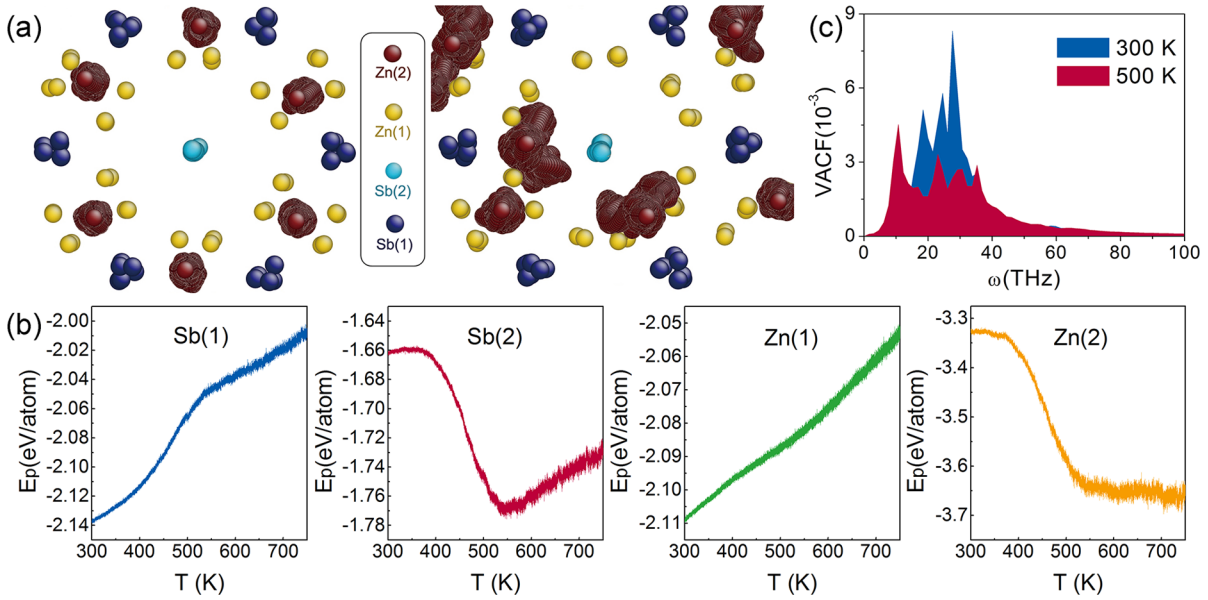

Figure 4. (a) Snapshots of β-Zn_4Sb_3 simulated at 300 K (left) and 500 K (right) from ⟨001⟩. Circles in four different colors show Zn at crystal sites [Zn(1)], Zn at glass-like sites [Zn(2)], and Sb at two different crystal sites [Sb(1) and Sb (2)], respectively. The clouds of Zn(2) positions show their vibrational trajectories at equilibrium. (b) Variation of the atomic potential energy during heating. (c) Power spectra of the velocity time-autocorrelation functions (VACF) of interstitial zinc atoms in β-Zn_4Sb_3 vs frequency at two different temperatures (300 and 500 K).[27]

thermal conductivity, its phase transition temperature (251 K), and its lattice thermal conductivity. All values were in good agreement with previous studies.[23,36]

The change in atomic potential energy (E_p) is a direct index of structural stability. Figure 4b shows that the slope of E_p changes twice, at 400 and 550 K. Sb(1) and Zn(1) atoms become less stable (E_p increases), while Sb(2) and Zn(2) become more stable (E_p decreases) with increasing temperature below 550 K, in agreement with our experimental observations on bond length variation shown in Figure 3f,g, and owing to diffusion of Zn atoms toward more energetically favorable positions. In contrast, the change in slope at 400 K is related to a subtler but remarkable transition that manifests itself in the onset of fast Zn diffusion. After about 550 K, the slope of $E_p(T)$ is similar to that observed before 400 K, which shows that β-Zn_4Sb_3 recovers its stability.

Structural analyses (Figure 3) confirm the migration of Zn atoms into glass-like Zn(2) sites, coexisting with the ones staying at Zn(1) crystal sites. This is also consistent with recent experimental observations on the self-diffusion in β-Zn_4Sb_3.[37] To understand the effects of such structural instability on thermal conduction, we computed the velocity time autocorrelation functions (VACF), whose power spectrum is proportional to the vibrational density of states; this, in turn, describes the energy distribution of heat carriers (phonons). In Figure 4c it can be seen that peaks located in the range from 10 to 70 THz are very strongly affected by an increase of temperature from 300 to 500 K, in stark contrast with the typical behavior of crystalline solids. Alternatively, this can be interpreted as a source of significant phonon anharmonicity, a factor known to be very influential in reducing the thermal conductivity.[38,39]

Being defect-free at the macro and micro levels is a precondition for β-Zn_4Sb_3 to obtain high performance at high temperature. Figure 5a shows the macroscopic and microscopic appearance of our SP sample, which is nearly dense. The fracture surface is clean with no visible defects such as pores. The XRD results in Figure 5b show that ZnSb reacts with Zn to form β-Zn_4Sb_3 at 570 K and such reaction does not occur at 560 K. The DSC curves in Figure 5c show a significant inflection point at about 425 K for the SP sample. Subsequently, there is no obvious change in the interval from 425 to 500 K. This onset temperature of 425 K is reasonable since the decomposition of β-Zn_4Sb_3 has been found before below 500 K.[15,20] The endothermic peak at about 765 K corresponds to the $\beta \rightarrow \gamma$ phase transition. This phase transition peak is also found in the mixture of ZnSb and Zn powders, which means that the reaction (1) is indeed reversed before 765 K. The inflection point at 565 K confirms that 565 K is a more precise reaction equilibrium temperature for ZnSb and Zn. After 565 K, β-Zn_4Sb_3 recovers its thermodynamic stability. We also used HRTEM to further study the stability of β-Zn_4Sb_3. A heat treatment following rapid cooling can preserve high-temperature microstructure even after samples have been cooled down to room temperature, as confirmed in a previous report.[40] Figure 5d shows the microstructure of β-Zn_4Sb_3 after different heat treatments following rapid cooling. Grain boundaries and inner grains are both clear at 300 K. After a 523 K heat treatment, nanostructures with characteristic sizes around 30 nm are found in the inner grain. These nanostructures are derived from the decomposition of β-Zn_4Sb_3, which has been confirmed in a previous study by some of the authors.[40] The decomposition products were also analyzed using energy-dispersive spectrometry (EDS) and fast Fourier transform (FFT), and the results are shown in Figure 5e. The distribution of Zn(hcp) shows that it prefers grain boundaries to the interior of the grains. In contrast, ZnSb is generated inside the grains. When the heat treatment temperature is raised to 623 K, the average size of nanostructures falls to 10 nm. Finally, these nanostructures disappear after 5 h of heat treatment at 723 K, which suggests that any damage caused by decomposition has been completely repaired. The emergence of nanostructures is one of the big contributors to the drop in thermal conductivity after 425 K. Conversely, their disappearance leads to the slight rise of

dx.doi.org/10.1021/ja410605f | J. Am. Chem. Soc. 2014, 136, 1497−1504

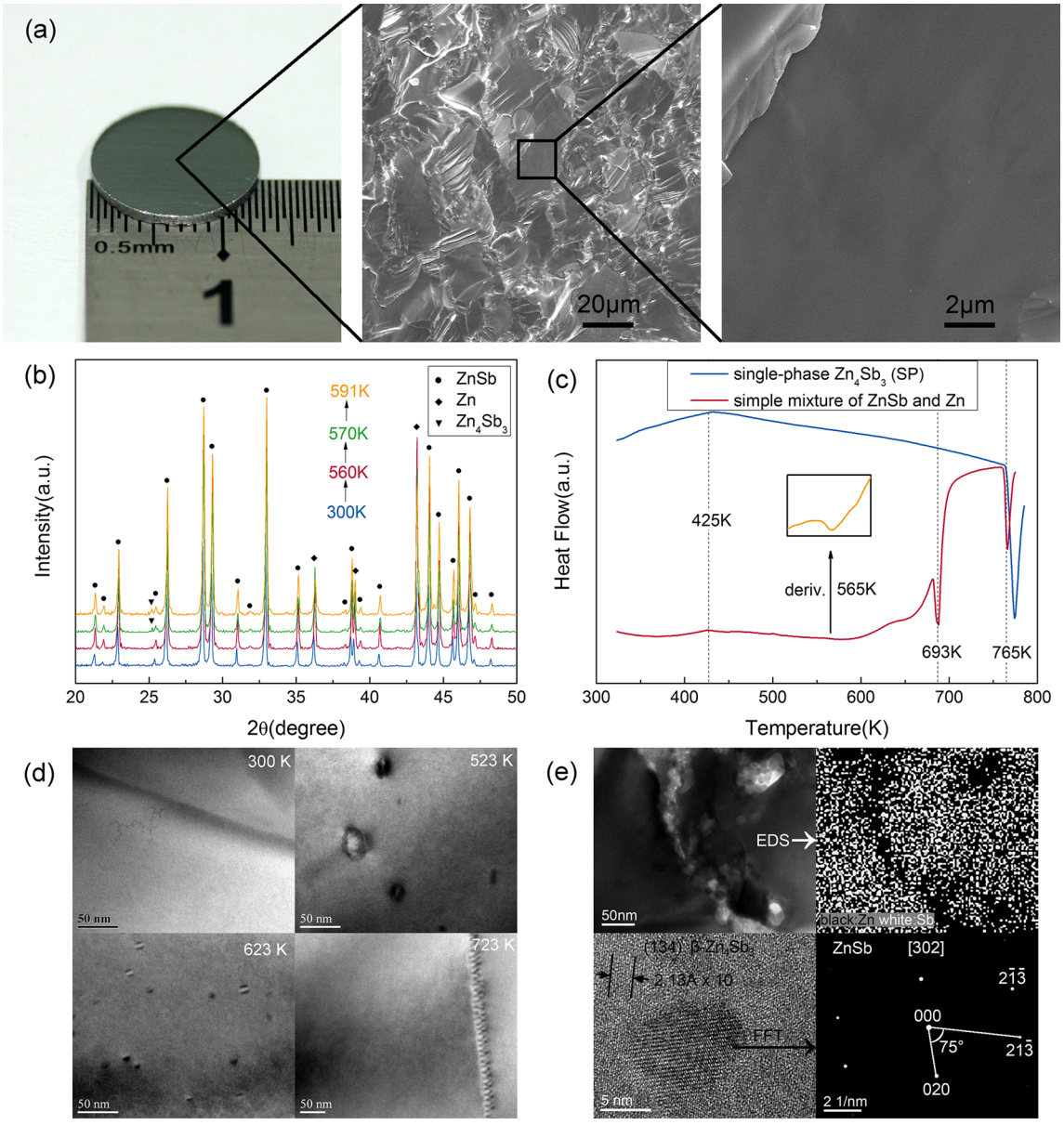

Figure 5. Thermodynamic stability and transformation kinetics of β-Zn_4Sb_3. (a) Macroscopic and microscopic appearance of the SP sample. (b) XRD results of the ZnSb and Zn mixtures. (c) DSC curves of a SP sample as well as ZnSb and Zn powder mixtures. (d) Microstructure of β-Zn_4Sb_3 after different heat treatments following rapid cooling. (e) Products of the decomposition of β-Zn_4Sb_3 after heat treatment (523 K) following rapid cooling; EDS and FFT are used to analyze composition.

κ_L(ZR) after 565 K. However, this phenomenon is not enough to increase κ_L(SP) due to the presence of Zn(1) vacancies with increasing temperature.

The time−temperature−transformation (TTT) curve of β-Zn_4Sb_3 can be described in the light of the above analysis. As seen in Figure 6, β-Zn_4Sb_3 is kinetically trapped under 425 K due to the high activation energy for Zn diffusion. If we heat the β-Zn_4Sb_3 sample along red curve to a temperature over 425 K, part of the Zn(1)−Sb(1) bonds break, and the migration of Zn atoms speeds up. Such migration of Zn atoms leads to fluctuations in composition. Some zones become Zn rich, which allows nano-Zn(hcp) or Zn(hcp) precipitates to appear. Some Zn-poor zones transform into the ZnSb phase and nano-ZnSb grows. When the temperature reaches 565 K, the free-energy balance changes and Zn(hcp) begins to react with ZnSb, and then the nanostructures shrink, and β-Zn_4Sb_3 becomes thermodynamically stable. If β-Zn_4Sb_3 decomposes too much at 425 K-565 K, resynthesis will be limited, and thermoelectric performance will suffer significantly at high temperature. The optimal temperature range for applications is between 565 and 765 K, and a nearly dense sample can be kept stable at such temperature if Zn evaporation can be sealed off. We conclude that the stability of β-Zn_4Sb_3 is a key determinant for the thermoelectric performance of SP sample at high temperature.

■ CONCLUSIONS

The thermodynamic character of β-Zn_4Sb_3 evolves from kinetically trapped to metastable and then to stable with increasing temperature. Around 425 K there is a first transition where superionic diffusion is activated. The weakening of Zn(1)−Sb(1) bonds allows significant diffusive motion of Zn atoms and generates a large amount of Zn(1) vacancies and

dx.doi.org/10.1021/ja410605f | J. Am. Chem. Soc. 2014, 136, 1497−1504

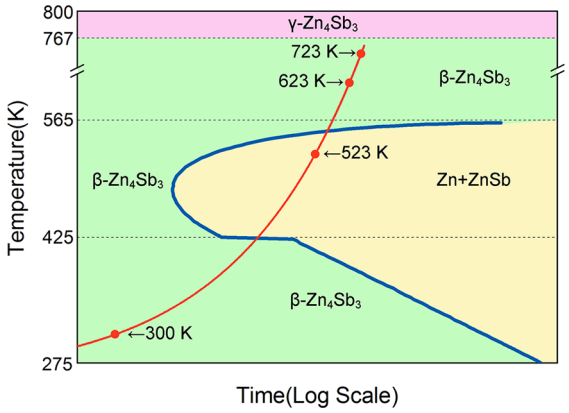

Figure 6. Schematic of the TTT curve for β-Zn_4Sb_3. $T_{kinetic}$ ~ 425 K corresponds to the onset of superionic diffusion of Zn and more rapid decomposition; T_{thermo} = 565 K corresponds to the lower bound of absolute thermodynamic stability of β-Zn_4Sb_3; a red line indicates the heating path; red dots correspond to the temperature in Figure 5d.

interstitial atoms. The "fluidity" of Zn atoms leads to additional anharmonic phonon scattering and reduces the efficiency of heat conduction by phonons. These result in a significant decline of thermal conductivity above 425 K. On the other hand, carrier transport properties are preserved. The decomposition of β-Zn_4Sb_3 is a time-dependent process, requiring diffusion of Zn and nucleation and growth of Zn(hcp) precipitates, which leads to degradation of the thermoelectric performance over time. 565 K is a second transition temperature, marking the onset of stability. The damage caused by decomposition in the metastable state can be repaired above this point, allowing excellent thermoelectric performance above 693 K: the ZT of our SP sample attains 1.4 at 748 K. The present comprehensive study is expected not only to be useful for explaining the excellent thermoelectric performance of β-Zn_4Sb_3 but also to provide insight for the search for new high-temperature thermoelectrics, as thermodynamic stability is a prerequisite for achieving functional performance that does not degrade with time.

AUTHOR INFORMATION

Corresponding Authors

gjqiao@mail.xjtu.edu.cn
zwangzhao@gmail.com
liju@mit.edu

Notes

The authors declare no competing financial interest.

ACKNOWLEDGMENTS

The authors thank Maud Giot, Guilhem Dezanneau, and Yang Hu at École Centrale de Paris for assistance with the structure refinement, Shuo Chen at Boston College for useful advice, and Kai Chen at Xi'an Jiaotong University for useful discussions. Use of the Advanced Photon Source at Argonne National Laboratory was supported by the U.S. DOE Office of Science under contract no. DE-AC02-06CH11357. This work has been supported by National Basic Research Program of China (grant nos. 2012CB619402 and 2014CB644003) and National Natural Science Foundation of China (11204228). JL acknowledges support by NSF DMR-1240933 and DMR-1120901.

REFERENCES

(1) Tritt, T. M.; Subramanian, M. A. *MRS Bull.* **2006**, *31*, 188.
(2) Harman, T. C.; Taylor, P. J.; Walsh, M. P.; LaForge, B. E. *Science* **2002**, *297*, 2229.
(3) Venkatasubramanian, R.; Siivola, E.; Colpitts, T.; O'Quinn, B. *Nature* **2001**, *413*, 597.
(4) Dresselhaus, M. S.; Chen, G.; Tang, M. Y.; Yang, R.; Lee, H.; Wang, D.; Ren, Z.; Fleurial, J.-P.; Gogna, P. *Adv. Mater.* **2007**, *19*, 1043.
(5) Hsu, K. F.; Loo, S.; Guo, F.; Chen, W.; Dyck, J. S.; Uher, C.; Hogan, T.; Polychroniadis, E. K.; Kanatzidis, M. G. *Science* **2004**, *303*, 818.
(6) Vineis, C. J.; Shakouri, A.; Majumdar, A.; Kanatzidis, M. G. *Adv. Mater.* **2010**, *22*, 3970.
(7) Poudel, B.; Hao, Q.; Ma, Y.; Lan, Y.; Minnich, A.; Yu, B.; Yan, X.; Wang, D.; Muto, A.; Vashaee, D.; Chen, X.; Liu, J.; Dresselhaus, M. S.; Chen, G.; Ren, Z. *Science* **2008**, *320*, 634.
(8) Poudeu, P. F. R.; D'Angelo, J.; Downey, A. D.; Short, J. L.; Hogan, T. P.; Kanatzidis, M. G. *Angew. Chem., Int. Ed.* **2006**, *45*, 3835.
(9) Amatya, R.; Ram, R. J. *J. Electron. Mater.* **2012**, *41*, 1011.
(10) Mozharivskyj, Y.; Pecharsky, A. O.; Bud'ko, S.; Miller, G. J. *Chem. Mater.* **2004**, *16*, 1580.
(11) Cox, C. A.; Toberer, E. S.; Levchenko, A. A.; Brown, S. R.; Snyder, G. J.; Navrotsky, A.; Kauzlarich, S. M. *Chem. Mater.* **2009**, *21*, 1354.
(12) Snider, T. S.; Badding, J. V.; Schujman, S. B.; Slack, G. A. *Chem. Mater.* **2000**, *12*, 697.
(13) Pomrehn, G. S.; Toberer, E. S.; Snyder, G. J.; van de Walle, A. *Phys. Rev. B* **2011**, *83*, 094106.
(14) Pomrehn, G. S.; Toberer, E. S.; Snyder, G. J.; van de Walle, A. *J. Am. Chem. Soc.* **2011**, *133*, 11255.
(15) Pedersen, B. L.; Iversen, B. B. *Appl. Phys. Lett.* **2008**, *92*, 161907.
(16) Yin, H.; Pedersen, B. L.; Iversen, B. B. *Eur. J. Inorg. Chem.* **2011**, 2733.
(17) Yin, H.; Christensen, M.; Pedersen, B. L.; Nishibori, E.; Aoyagi, S.; Iversen, B. B. *J. Electron. Mater.* **2010**, *39*, 1957.
(18) Mozharivskyj, Y.; Janssen, Y.; Harringa, J. L.; Kracher, A.; Tsokol, A. O.; Miller, G. J. *Chem. Mater.* **2006**, *18*, 822.
(19) Zhang, L. T.; Tsutsui, M.; Ito, K.; Yamaguchi, M. *J. Alloys Compd.* **2003**, *358*, 252.
(20) Schlecht, S.; Erk, C.; Yosef, M. *Inorg. Chem.* **2006**, *45*, 1693.
(21) Sun, Y.; Christensen, M.; Johnsen, S.; Nong, N. V.; Ma, Y.; Sillassen, M.; Zhang, E.; Palmqvist, A. E. C.; Bottiger, J.; Iversen, B. B. *Adv. Mater.* **2012**, *24*, 1693.
(22) Ahn, J. H.; Oh, M. W.; Kim, B. S.; Park, S. D.; Min, B. K.; Lee, H. W.; Shim, Y. J. *Mater. Res. Bull.* **2011**, *46*, 1490.
(23) Snyder, G. J.; Christensen, M.; Nishibori, E.; Caillat, T.; Iversen, B. B. *Nat. Mater.* **2004**, *3*, 458.
(24) May, A. F.; Toberer, E. S.; Saramat, A.; Snyder, G. J. *Physical Review B* **2009**, *80*, 125205 .
(25) Johnsen, S.; He, J.; Androulakis, J.; Dravid, V. P.; Todorov, I.; Chung, D. Y.; Kanatzidis, M. G. *J. Am. Chem. Soc.* **2011**, *133*, 3460.
(26) Girard, S. N.; He, J.; Zhou, X.; Shoemaker, D.; Jaworski, C. M.; Uher, C.; Dravid, V. P.; Heremans, J. P.; Kanatzidis, M. G. *J. Am. Chem. Soc.* **2011**, *133*, 16588.
(27) Li, X.; Carrete, J.; Lin, J.; Qiao, G.; Wang, Z. *Appl. Phys. Lett.* **2013**, *103*, 103902.
(28) Hammersley, A. P. *ESRF Internal Report, ESRF97HA02T*; European Synchrotron Radiation Facility: Grenoble, France, 1997.
(29) Larson, A. C.; Dreele, R. B. V. *Los Alamos National Laboratory Report (LAUR)*; Los Alamos National Laboratory: Los Alamos, NM, 2004; p 86.
(30) Caillat, T.; Fleurial, J. P.; Borshchevsky, A. *J. Phys. Chem. Solids* **1997**, *58*, 1119.
(31) Plimpton, S. *J. Comput. Phys.* **1995**, *117*, 1.
(32) Schweika, W.; Hermann, R. P.; Prager, M.; Persson, J.; Keppens, V. *Phys. Rev. Lett.* **2007**, *99*, 125501.
(33) Toberer, E. S.; Sasaki, K. A.; Chisholm, C. R. I.; Haile, S. M.; Goddard, W. A.; Snyder, G. J. *Phys. Status Solidi RRL* **2007**, *1*, 253.

(34) Cargnoni, F.; Nishibori, E.; Rabiller, P.; Bertini, L.; Snyder, G. J.; Christensen, M.; Gatti, C.; Iversen, B. B. *Chem.—Eur. J.* **2004**, *10*, 3861.
(35) Li, G.; Li, Y.; Yang, X.; Tong, Y.; Zhou, A.; Liu, L.; Zhai, P. *J. Electron. Mater.* **2011**, *40*, 1158.
(36) Souma, T.; Nakamoto, G.; Kurisu, M. *J. Alloys Compd.* **2002**, *340*, 275.
(37) Løvvik, O. M.; Rauwel, P.; Prytz, Ø. *Comput. Mater. Sci.* **2011**, *50*, 2663.
(38) Ziman, J. M. *Electrons and Phonons: The Theory of Transport Phenomena in Solids*; Oxford University Press, Oxford, 1960.
(39) Sievers, A. J.; Takeno, S. *Phys. Rev. Lett.* **1988**, *61*, 970.
(40) Lin, J.; Qiao, G.; Ma, L.; Ren, Y.; Yang, B.; Fei, Y.; Lei, L. *Appl. Phys. Lett.* **2013**, *102*, 163902.